S14-02

RECENT PROGRESS IN THE ANALYSIS OF ICED AIRFOILS AND WINGS

by

p. 10

Tuncer Cebeci*, Hsun H. Chen**, Kalle Kaups† and Sue Schimke††
Aerospace Engineering Department,
California State University, Long Beach

Abstract

Recent work on the analysis of iced airfoils and wings is described. Ice shapes for multi-element airfoils and wings are computed using an extension of the LEWICE code that was developed for single airfoils. The aerodynamic properties of the iced wing are determined with an interactive scheme in which the solutions of the inviscid flow equations are obtained from a panel method and the solutions of the viscous flow equations are obtained from an inverse three-dimensional finite-difference boundary-layer method. A new interaction law is used to couple the inviscid and viscous flow solutions.

The newly developed LEWICE multielement code is applied to a high-lift configuration to calculate the ice shapes on the slat and on the main airfoil and on a four-element airfoil.

The application of the LEWICE wing code to the calculation of ice shapes on a MS-317 swept wing shows good agreement with measurements. The interactive boundary-layer method is applied to a tapered iced wing in order to study the effect of icing on the aerodynamic properties of the wing at several angles of attack.

1.0 Introduction

In recent years there has been considerable research activity in the area of aircraft icing to combat the adverse effects of leading-edge ice formation on fixed and rotary wing aircraft and on engine intakes. Computational work and related experimental studies have been initiated and are being carried out under the NASA Aircraft Icing Research Program to develop and validate a series of mutually compatible computer codes to predict the details of an aircraft icing encounter.[1] The papers presented each year at the the AIAA Aerospace Sciences Meeting and the papers presented in this symposium show that indeed much progress has been made in this area.

In this paper we report a summary of our progress in predicting ice shapes on airfoils and wings and in determining the effect of ice formation on aerodynamic performance degradation. For airfoil flows, our research has led to improvements in the LEWICE code[2] for predicting leading-edge ice formation[3] and to the development of an interactive boundary-layer (IBL) method[4] for determining the increase in drag and loss of lift of airfoils[5,6] and helicopter blades[7] due to icing. This capability for predicting ice shapes on airfoils has also been extended by the authors to include airfoils with slats, and very recently to multielement airfoils so that ice shapes on the main airfoil and on the flap can be computed as well as on the slat. This will permit the effects of icing on high-lift configurations to be computed using the interactive boundary-layer method recently developed by Cebeci et al.[8]

For wing flows, our research followed a similar path, concentrating on the development of (1) a three-dimensional version of the LEWICE code, (2) a three-dimensional interactive boundary-layer (IBL) method for iced wings, and (3) the coupling of the IBL method to the LEWICE code to determine the ice shapes and their effects on lift, drag and moment coefficients for wing flows.

The progress to date for airfoil flows is described in several papers. For this reason the present paper concentrates mainly on three-dimensional flows and describes the extension to wing flows of the combined LEWICE/IBL procedure developed for airfoils. Section 2 describes the method for calculating ice shapes on the leading edge of a wing and presents a comparison between calculated and experimental results. Section 3 describes the interactive boundary-layer method for computing three-dimensional flows on iced wings. In addition, this section presents the results obtained from the application of this method to a NASA MS 317 tapered wing with ice and to an unswept NACA 0012 wing without ice. In each case, the inviscid and viscous flow equations are solved interactively to determine the increase in drag due to ice and to compare the calculated pressure coefficients with measured values. Section 4 presents recent results obtained for multi-element airfoils and is followed by concluding remarks.

2.0 Extension of LEWICE to Wings and Its Validation

The extension of the LEWICE airfoil code to wings is not so straightforward. There are several possible approaches that can be pursued. In each approach the flowfield calculations should be performed in principle using a three-dimensional inviscid method, and the impingement pattern of the water droplets on the surface should be determined by performing trajectory calculations for the three components of the velocity obtained from the inviscid method. The heart of the LEWICE code, however, is the third module that contains the quasi-steady-state surface heat transfer analysis in which mass and energy equations are solved for a two-dimensional flow in order to determine the ice shape and size. The extension of this module to three-dimensional flows would require the heat balance equation, developed for airfoil flows, to be modified to wing flows. And, as discussed in Ref. 9, this can only be done with the help of experimental data that presently do not exist. As a first step, it is best to leave the heat balance in its

* Professor and Chairman.
** Associate Professor.
† Research Professor.
†† Research Associate.

two-dimensional form and assume it to apply to a three-dimensional body expressed in an equivalent two-dimensional form. One approach, followed by Potapczuk and Bidwell,[10] is to perform the trajectory calculations for a three-dimensional flowfield and apply them along the streamlines on the wing. Another approach, followed in Ref. 9, is to approximate the 3-D wing by an equivalent yawed infinite wing at each spanwise station. In this case, the flowfield is calculated by a three-dimensional panel method and the particle trajectories calculated for flow normal to the leading edge subject to the infinite swept-wing assumption. Another approach is to apply the LEWICE airfoil code to the streamwise cross-section of the wing. This approach has at least two alternatives, one of which is described in this paper. The accuracy of these three approaches and others depend on the angle of attack and the spanwise location of the airfoil section, and they require a careful evaluation through comparisons with experimental data.

2.1 Comparison of Measured Ice Shapes and Predictions Obtained with Yawed Wing Approximation

The calculated results obtained with the extension of the LEWICE airfoil code to wing flows by the method of Ref. 9 are shown in Figs. 1 and 2 together with the experimental results[11] on an MS-317 swept wing. A summary of test conditions used in the calculations are given in Table 1. Additional studies for other test conditions are in progress and will be reported later. The calculated ice shapes in Figs. 1 and 2 were obtained for the untapered wing with a MS-317 airfoil section defined streamwise with a sweep angle of 30° and an aspect ratio of six. All trajectory and ice accretion calculations were carried out for inviscid flow computed on the mid-semispan section where the spanwise pressure gradient was negligible. All calculations were performed for one time step to save computer time, which is approximately 7 minutes per run on the Cray computer. The increase in time, in comparison with the two-dimensional case, is primarily due to the trajectory calculations where, despite the yawed infinite wing approximations, the computation of the off-body velocities involves repeated large matrix multiplications in which all wing panels are represented.

Figure 1a shows a comparison of measured and calculated ice shapes for Run 8, which corresponds to T_∞ = 0°, α = 2°, t = 390 sec. As can be seen, the agreement between measured and calculated results is remarkably good. The calculated results for a calculation time of 1164 sec and for T_∞ = 0°F and α = 2° (Run 11) are shown in Fig. 1b and indicate reasonable agreement with measurements despite the one time step used in the calculations. It is expected that the ice growth will have some effect on the velocity field and on the calculated droplet impingement. A comparison of predicted and measured ice shapes obtained for T_∞ = 0°F at α = 8° for t = 390 and 1164 sec. (Runs 9 and 10) are shown in Figs. 1c and 1d, respectively. The agreement is again reasonable, keeping in mind that only one time step was used in the calculations.

The next set of studies was conducted for a slightly higher freestream temperature of T_∞ = 15°F, representing an icing condition for which

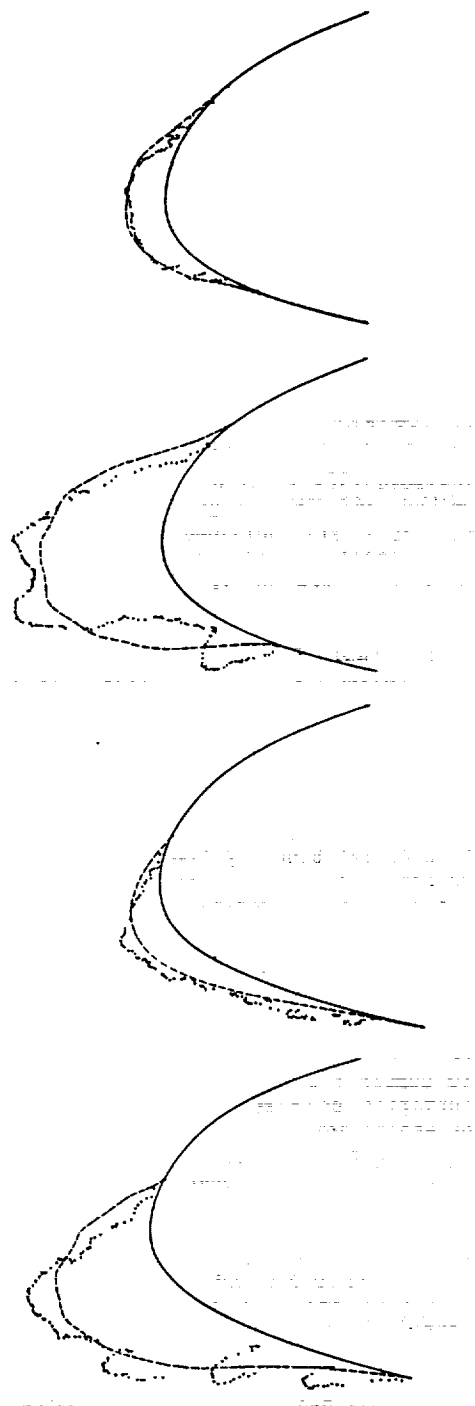

Fig. 1. Comparison of calculated (solid lines) and measured (dashed lines) ice shapes. Rime ice: (a) Run 8, (b) Run 11, (c) Run 9, (d) Run 10.

a mixed ice growth was observed. Run 7 in Fig. 2a for α = 2° and t = 390 sec. indicates good agreement between experiment and theory, except for some deviation on the upper surface. The results in Fig. 2b at the large time step of t = 1164 sec. (Run 1) are more or less in agreement in predicting the amount of ice accumulated, but they differ in predicting its shape. It is known from two-dimensional calculations that a large number of relatively short time steps are needed to predict horn-shaped ice for glaze ice. Since the mixed ice formation tends toward glaze ice shapes for

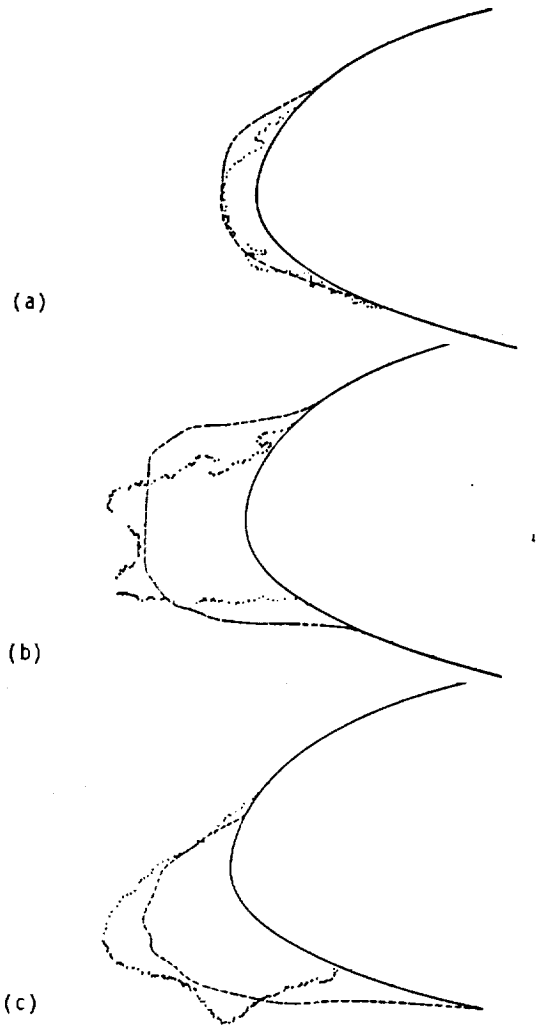

Fig. 2. Comparison of calculated (solid lines) and measured (dashed lines) ice shapes. Mixed ice: (a) Run 7, (b) Run 1, (c) Run 6.

Table 1. Test Conditions for MS-317 Ice Accretion Experiment of Ref. 8, V_∞ = 150 mph, d = 20 μm, LWC = 1.03 gm^{-3}.

Run	T_∞ (°F)	t (sec)	α (deg)	$(k_s/c)_1$
1	15	1164	2.0	0.00192
6	15	1164	8.0	0.00192
7	15	390	2.0	0.00192
8	0	390	2.0	0.00127
9	0	390	8.0	0.00127
10	0	1164	8.0	0.00127
11	0	1164	2.0	0.00127

large times, it is not surprising that one time step calculation is not sufficient to predict the actual growth of the ice shapes. Similar comments apply to Fig. 2c, where comparisons are for a large time step of t = 1164 sec. (Run 6), but at α = 8°.

2.2 Comparison of Measured Ice Shapes and Predictions Obtained with Strip Theory Approximation

Additional calculations were also performed with the LEWICE code to determine the ice shapes on the leading edge of the MS-317 swept wing discussed in the previous subsection. This time we used the strip theory approximation rather than the yawed wing approximation. We calculated the three-dimensional velocity field from the panel method and used the velocity distribution in the LEWICE code for the streamwise airfoil section. Figure 3 shows a comparison between the ice shapes computed with strip theory (2-D) and yawed wing (3-D) approximations together with the measured ice shape for run 11. As can be seen, both calculated ice shapes, at least for this run, agree reasonably well with experimental data. Additional studies are underway to further investigate the differences between the two procedures.

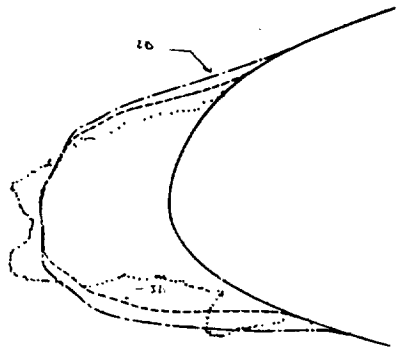

Fig. 3. Comparison of calculated ice shapes with experimental data. 2-D represents the ice shape with strip theory approximation and 3-D that with yawed wing approximation.

2.3 The Role of Wind Tunnel Effect on the Calculation of Ice Shapes

In general, infinite yawed wing conditions apply to the mid-semispan section of wings with an aspect ratio greater than about five. This approximation becomes progressively less accurate as the tip or the root of the wing is approached, but in most instances it can still provide reasonable answers. A point to remember about the use of this approximation with finite aspect ratio wings is that although the flow may have the desired characteristics, its lift is always less than the lift of a wing with infinite aspect ratio. This may lead to problems in comparing calculations with experimental data unless the aspect ratio or the pressure distribution is also given. If the pressure distribution is not available, the given angle of attack may not properly represent the experimental conditions. Similar problems may also arise in simulating wind-tunnel conditions by calculating the corrected incidence and lift coefficient in free air, because the trajectories in the two cases may be far from identical. One solution to the wind-tunnel problem, which may be the only acceptable solution for a swept wing spanning the tunnel, is to calculate the flowfield about the wing in the presence of the tunnel walls.

The comparisons between the calculated and experimental ice shapes presented in Subsections 2.1 and 2.2 were obtained for the icing conditions and angle of attack given in Table 1. Care, however, is required to perform the calculations as closely as possible to the stated experimental conditions. Even though the atmospheric icing conditions are properly defined in the LEWICE calculations, the angle observed in the wind tunnel together with the wing aspect ratio may

need to be different when the flowfield calculations are performed with the panel method for a free air model.

To investigate this possibility further, we have calculated the pressure distributions for a constant chord wing with MS-317 streamwise sections and with a 30° sweep, having a finite aspect ratio in free air and spanning the side walls of a wind tunnel, using the panel method of Ref. 12. The free air model was chosen to have an aspect ratio of 6 in order to reduce the root and tip effects at the mid-semispan location. It was found that the angle of attack of the free-air model had to be increased to 4° for the pressure distributions to match the experimental data of Bidwell[7] measured at 2° angle or attack in the wind tunnel. The 8° angle-of-attack case in Table 1 required an increase of 3.5° angle of attack in free air to obtain satisfactory agreement with the pressure distributions. Since there is some doubt about the flowfields being matched at the widely differing angles of attack in the wind tunnel and in free air, the flow was calculated about the wing in the wind tunnel. This requires additional paneling of the tunnel floor, ceiling and one sidewall, while taking advantage of one plane of symmetry. Figure 4 shows the calculated and measured pressure distributions at $\alpha = 2°$ in the wind tunnel compared with results from the calculations in free air at $\alpha = 2°$ and 4°. Agreement between the experimental data and the calculations for the wing in the wind tunnel is very good, considering that the calculated pressure distribution corresponds to inviscid pressure distribution and does not include any viscous effects. As can be seen, matching of free-air calculations with wind-tunnel data is a trial and error process. Studies are underway to extend these calculations to include a wing with ice. This is relatively easy, except for the longer computing times for the particle trajectories resulting from the large number of panels used in the calculation of the inviscid flowfield.

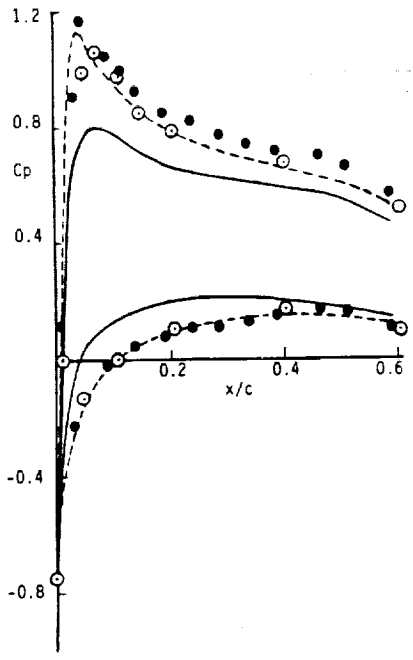

Fig. 4. Computed and experimental pressure distributions for the MS-317 airfoil. — denotes results for $\alpha = 2°$, free air, --- $\alpha = 4°$, free air. Symbol o denotes experimental results for $\alpha = 2°$, wing tunnel and o denotes calculated results for $\alpha = 2°$, wind tunnel.

3.0 Three-Dimensional Interactive Boundary-Layer Method

A complete description of the three-dimensional interactive boundary-layer method is described in Ref. 9 and is presented here for completeness.

As in two-dimensional flows, the interactive method for three-dimensional flows is based on the solutions of the inviscid and boundary-layer equations. An interface program, illustrated by Fig. 5, is placed between the inviscid and three-dimensional inverse boundary-layer methods to process the geometry and inviscid velocity data for input to the boundary-layer program. The basic input to this program is (1) the definition of the wing configuration that is used by a geometry subroutine to construct a nonorthogonal coordinate system and (2) the associated geometrical parameters, which consist of the geodesic curvatures and metric coefficients needed in the boundary-layer calculations. Some of the generated data is used later in a velocity subroutine to determine the inviscid velocity components at the boundary-layer grid points and to transform the inviscid velocity components on the surface, calculated in a Cartesian coordinate system, into the boundary-layer coordinate system. This operation consists of calculating dot products of velocity vectors as well as chordwise and spanwise interpolation. Further velocity and geometry data processing is carried out in a subroutine that separates the generated information into upper and lower surfaces of the wing for boundary-layer calculations.

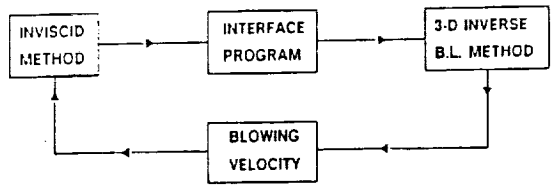

Fig. 5. The interactive boundary-layer method.

The above procedure is appropriate to wings without ice and has been used to compute transonic flows on wing/body configurations[18] where, since the wing leading edge was free of ice, there was no difficulty in generating solutions near the attachment line by constructing the nonorthogonal coordinate system and computing the geometrical properties of the wing. For a wing with ice, generation of the boundary-layer solutions near the leading edge can pose problems since the geodesic curvatures and metric coefficients must be determined for an irregular surface. In addition, the formulation of the interactive boundary-layer method developed for iced airfoils must take account of the three-dimensional nature of the flow. Thus, it is necessary to make changes in the strategy for solving the three-dimensional boundary-layer equations for an iced wing. These are considered below.

3.1 Boundary-Layer Equations

The three-dimensional boundary-layer equations for a nonorthogonal coordinate system are given in several references. With Reynolds stresses modeled by the eddy-viscosity concept, they can be written as,

$$\frac{\partial}{\partial x}(uh_2 \sin\theta) + \frac{\partial}{\partial z}(wh_1 \sin\theta) + \frac{\partial}{\partial y}(vh_1h_2 \sin\theta) = 0 \tag{1}$$

$$\frac{u}{h_1}\frac{\partial u}{\partial x} + \frac{w}{h_2}\frac{\partial u}{\partial z} + v\frac{\partial u}{\partial y} - K_1u^2\cot\theta + K_2w^2\operatorname{cosec}\theta + K_{12}uw = -\frac{\operatorname{cosec}^2\theta}{\rho h_1}\frac{\partial p}{\partial x} + \frac{\cot\theta\operatorname{cosec}\theta}{\rho h_2}\frac{\partial p}{\partial z} + \nu\frac{\partial}{\partial y}\left(b\frac{\partial u}{\partial y}\right) \tag{2}$$

$$\frac{u}{h_1}\frac{\partial w}{\partial x} + \frac{w}{h_2}\frac{\partial w}{\partial z} + v\frac{\partial w}{\partial y} - K_2w^2\cot\theta + K_1u^2\operatorname{cosec}\theta + K_{21}uw = \frac{\cot\theta\operatorname{cosec}\theta}{\rho h_1}\frac{\partial p}{\partial x} - \frac{\operatorname{cosec}^2\theta}{\rho h_2}\frac{\partial p}{\partial z} + \nu\frac{\partial}{\partial y}\left(b\frac{\partial w}{\partial y}\right) \tag{3}$$

Here x denotes the coordinate along the lines formed by the intersection of the wing surface and planes representing constant percent semispan; z is the coordinate along the constant percent chordlines that generate the wing surface, with chord defined as the maximum length line between leading edge and trailing edge. The third coordinate y denotes the direction normal to the wing surface, and the parameter h denotes the metric coefficients, with θ the angle between the coordinate lines x = const and z = const. For an orthogonal system, $\theta = \pi/2$. The parameters K_1 and K_2 are known as the geodesic curvatures of the curves z = const and x = const, respectively. Equations (1) to (3) are subject to the following boundary conditions

$$y = 0, \quad u = 0, \quad v = 0, \quad w = 0 \tag{4a}$$

$$y = \delta, \quad u = u_e(x,z), \quad w = w_e(x,z) \tag{4b}$$

The solution of the above equations also requires initial conditions on two intersecting planes; those in the (y,z) plane at a specified chordwise location are determined from the solutions of the equations discussed in Subsection 4.3. Those on the (x,y) plane, at a specified spanwise location $z = z_0$, with z_0 corresponding to, say, the root location, are determined from the solutions of the quasi-three-dimensional form of Eqs. (1) to (3) with all derivatives with respect to z neglected, that is,

$$\frac{\partial}{\partial x}(uh_2\sin\theta) + \frac{\partial}{\partial y}(vh_1h_2 \sin\theta) = 0 \tag{5}$$

$$\frac{u}{h_1}\frac{\partial u}{\partial x} + v\frac{\partial u}{\partial y} - K_1u^2\cot\theta + K_2w^2\operatorname{cosec}\theta + K_1uw = -\frac{\operatorname{cosec}^2\theta}{\rho h_1}\frac{\partial p}{\partial x} + \nu\frac{\partial}{\partial y}\left(b\frac{\partial u}{\partial y}\right) \tag{6}$$

$$\frac{u}{h_1}\frac{\partial w}{\partial x} + v\frac{\partial w}{\partial y} - K_2w^2\cot\theta + K_1u^2\operatorname{cosec}\theta + K_{21}uw = \frac{\cot\theta\operatorname{cosec}\theta}{\rho h_1}\frac{\partial p}{\partial x} + \nu\frac{\partial}{\partial y}\left(b\frac{\partial w}{\partial y}\right) \tag{7}$$

subject to the same boundary conditions given in Eq. (4).

3.2 Interaction Law

To account for possible flow separation, as in two-dimensional flows, we use the interaction law of Veldman[13] where, for airfoil flows, the edge velocity is expressed as the sum of an inviscid velocity $u_e^0(x)$ and perturbation velocity $\delta u_e(x)$ due to viscous effects, that is,

$$u_e(x) = u_e^0(x) + \delta u_e(x) \tag{8}$$

The perturbation velocity is given by the Hilbert integral

$$\delta u_e(x) = \frac{1}{\pi}\int_{x_a}^{x_b}\frac{d}{d\sigma}(u_e\delta^*)\frac{d\sigma}{x-\sigma} \tag{9}$$

in the interaction region (x_a, x_b).

To extend this inverse formulation to three-dimensional flows, it is necessary that the two-dimensional interaction formula given by Eq. (9) be either modified to account for the interaction in the x- and z-directions or be replaced by another formulation which provides a relationship between displacement surface and external velocity. Here we use the former approach, as described in Ref. 14, and first generate an initial displacement surface by solving the quasi-three-dimensional boundary-layer equations subject to the boundary conditions given by Eqs. (4) and (8) with the external velocity distribution $u_e^0(x)$ obtained from the panel method. The second step involves interaction between the inviscid flow equations and the quasi-three-dimensional flow equations. As in two-dimensional flows, the solutions of the boundary-layer equations are used to compute distributions of blowing velocity on the surface, and these allow the inviscid flow solutions to be updated. In step three, after the calculation of the initial conditions in the (y,z) and (x,y) planes, the fully three-dimensional boundary-layer equations are solved with the external velocity components resulting from step two. As before, the spanwise velocity component is assumed to correspond to its inviscid value. The viscous flow solutions are obtained by marching in the spanwise direction at each advancing chordwise location. This represents the first phase in an interactive loop that involves the fully three-dimensional boundary-layer equations. In the subsequent phases, as before, the blowing velocity distribution is used to obtain improved inviscid flow solutions, so the fully three-dimensional boundary-layer equations are solved for iced wings as for clean wings in transonic flow.[14]

The viscous effects in the spanwise component w_e are assumed to be second order, although their neglect is contrary to the irrotationality condition. However, trial calculations involving variations of both velocity conditions showed that errors were smaller than those associated with the convergence of the solutions.

3.3 Transformed Equations

As in two-dimensional flows, we express the boundary-layer equations in transformed variables for computational purposes. At first, when the equations are solved for a prescribed external velocity distribution (standard problem), we use the Falkner-Skan transformation and a modified version of this transformation for the inverse mode. In the former case, the independent variables are defined by

$$x = x, \quad z = z, \quad \eta = \left(\frac{u_e}{\nu s}\right)^{1/2} y, \quad s = \int_0^x h_1 dx \tag{10}$$

For the dependent variables u, v and w, we introduce a two-component vector potential such that

$$uh_2 \sin\theta = \frac{\partial \psi}{\partial y}, \quad wh_1 \sin\theta = \frac{\partial \Phi}{\partial y},$$

$$vh_1 h_2 \sin\theta = -\left(\frac{\partial \psi}{\partial x} + \frac{\partial \Phi}{\partial z}\right) \tag{11}$$

In addition, dimensionless parameters f and g are defined by

$$\psi = (u_e \nu s)^{1/2} h_2 \sin\theta f(x,z,\eta) \tag{12}$$

$$\Phi = (u_e \nu s)^{1/2} \frac{u_o}{u_e} h_1 \sin\theta g(x,z,\eta)$$

$$(bf'')' + ef'' + m_2(f')^2 + m_5 f'g' + m_8(g')^2 + m_{11} = m_{10} f' \frac{\partial f'}{\partial x} + m_7 g' \frac{\partial f'}{\partial z} \tag{13}$$

$$(bg'')' + eg'' + m_4 f'g' + m_3(g')^2 + m_9(f')^2 + m_{12} = m_{10} f' \frac{\partial g'}{\partial x} + m_7 g' \frac{\partial g'}{\partial z} \tag{14}$$

$$e' = m_1 f' + m_6 g' + m_{10} \frac{\partial f'}{\partial x} + m_7 \frac{\partial g'}{\partial z} \tag{15}$$

The coefficients m_1 to m_{12} are defined in Ref. 9.

In terms of transformed variables, boundary conditions given by Eq. (4) become

$$\eta = 0: \quad f = g = f' = g' = 0$$

$$\eta = \eta_e: \quad f' = 1, \quad g' = \frac{w_e}{u_o} \tag{16}$$

The form of the transformed quasi-three-dimensional equations is identical to the form of Eqs. (13) to (15), except for small differences discussed in Ref. 9.

To solve the equations in the inverse mode, we define independent variables by

$$x = x, \quad z = z, \quad Y = \left(\frac{u_o}{\nu s}\right)^{1/2} y, \quad s = \int_0^x h_1 dx \tag{17}$$

and relate the vector potentials ψ and Φ to f and g by

$$\psi = (u_o \nu s)^{1/2} h_2 \sin\theta f(x,z,\eta)$$

$$\Phi = (u_o \nu s)^{1/2} h_1 \sin\theta g(x,z,\eta) \tag{18}$$

and with a prime now denoting differentiation with respect to Y and $\bar{u}_e$ and $\bar{w}_e$ denoting edge velocity components normalized by reference velocity u_o, Eqs. (1) to (3), with e' defined by Eq. (15) and m's given in Ref. 9, are written as

$$(bf'')' + ef'' + m_2[(f')^2 - (\bar{u}_e)^2] + m_5[f'g' - \bar{u}_e\bar{w}_e] + m_8[(g')^2 - (\bar{w}_e)^2] = m_{10}\left(f' \frac{\partial f'}{\partial x} - \bar{u}_e \frac{\partial \bar{u}_e}{\partial x}\right) + m_7\left(g' \frac{\partial f'}{\partial z} - \bar{w}_e \frac{\partial \bar{u}_e}{\partial z}\right) \tag{19}$$

$$(bg'')' + eg'' + m_3[(g')^2 - (\bar{w}_e)^2] + m_4[f'g' - \bar{u}_e\bar{w}_e] + m_9[(f')^2 - (\bar{u}_e)^2] = m_{10}\left(f' \frac{\partial g'}{\partial x} - \bar{u}_e \frac{\partial \bar{w}_e}{\partial x}\right) + m_7\left(g' \frac{\partial g'}{\partial z} - \bar{w}_e \frac{\partial \bar{w}_e}{\partial z}\right) \tag{20}$$

The transformed boundary conditions for the system of Eqs. (19) and (20), with u_e given by Eq. (8) and with w_e corresponding to its inviscid value, are

$$\eta = 0: \quad f = g = f' = g' = 0 \tag{21a}$$

$$\eta = \eta_e: \quad f' = \bar{u}_e, \quad g' = \bar{w}_e \tag{21b}$$

The quasi-three-dimensional form of the equations, which are subject to the boundary conditions given by Eq. (21), are obtained from the above equations by setting

$$\frac{\partial f'}{\partial z} = \frac{\partial g'}{\partial z} = \frac{\partial \bar{u}_e}{\partial z} = \frac{\partial \bar{w}_e}{\partial z} = 0 \quad \text{and} \quad m_6 = 0 \tag{22}$$

To generate the initial conditions near the leading edge of the iced wing, we use quasi-three-dimensional boundary-layer equations expressed in the inverse mode given by

$$(bf'')' + ef'' + m_2[(f')^2 - (\bar{u}_e)^2] + m_5(f'g' - \bar{u}_e\bar{w}_e) + m_8[(g')^2 - (\bar{w}_e)^2] = m_{10}\left(f' \frac{\partial f'}{\partial x} - \bar{u}_e \frac{\partial \bar{u}_e}{\partial x}\right) \tag{23}$$

$$(bg'')' + eg'' + m_3[(g')^2 - (\bar{w}_e)^2] + m_4(f'g' - \bar{u}_e\bar{w}_e) + m_9[(f')^2 - (\bar{u}_e)^2] = m_{10}\left(f' \frac{\partial g'}{\partial x} - \bar{u}_e \frac{\partial \bar{w}_e}{\partial x}\right) \tag{24}$$

$$e' = m_1 f' + m_{10} \frac{\partial f'}{\partial x} \tag{25}$$

The above equations can be further simplified if we assume that two adjacent defining sections of a wing are connected by straight line development, as commonly used in the wing design. This

feature simplifies the problem of shaping the metal for a wing surface. As a consequence, we can neglect the geodesic curvature of x = constant lines, namely K_2, and thus set $m_3 = m_8 = 0$. From the definitions of m_4 and m_5, it can be seen that as a result of the above assumption, these two terms are also small and can be neglected. We further assume that the local variations in cross sections in the spanwise direction are small. Examination of the terms m_1, m_2 and m_9 for a typical wing shows that m_2 reaches a value less than 0.1 very close to the leading edge ($x/c < 0.01$) and m_9 reaches a maximum value of 0.2. However, their magnitudes rapidly decrease with increasing x and reach a very small value at $x/c < 0.1$. This behavior allows us to neglect m_2 and m_9 in the equations and set $m_1 = 1/2$.

3.4 Solution Procedure

A detailed description of the solution procedure will be reported separately. Briefly, the boundary-layer equations expressed in terms of transformed variables are solved with Keller's two-point finite-difference method[15] (box scheme) with boundary conditions expressed in inverse form with the interaction law described in Subsection 3.2. Depending on the complexity of the flow-field, two forms of the box scheme are employed. In regions where all velocity components are positive, the regular box scheme is used. In regions of either a negative spanwise velocity component or negative streamwise velocity component, the zig-zag box scheme described in Ref. 15 is used.

3.5 Performance Degradation of an Iced Tapered Wing

The interactive boundary-layer method of Section 3 was used to study the performance degradation of an iced wing having MS-317 airfoil streamwise sections, an aspect ratio of 3.43, and a taper ratio of 0.4. Icing conditions were chosen to correspond to those in Runs 8 and 11, shown in Table 1. The pressure distribution on the wing was computed at four locations defined by the midsection of each wing-section with a hundred panels on each defining airfoil section. The ice shapes corresponding to this pressure distribution were computed with the method of Section 2 in the middle of each wing section and were used to distribute ice along the leading edge of the tapered wing. The computed ice shapes for $\alpha = 2°$ were then assumed to be the same for all angles of attack on the wing in the investigation of the performance degradation of the wing due to ice shapes corresponding to the atmospheric conditions given in Runs 8 and 11. At a specified angle of attack, with the defined ice shapes along the leading-edge of the wing, calculations were performed with the method of Section 3; that is, inviscid flow calculations performed for an iced wing were followed by the inverse three-dimensional boundary-layer calculations to determine the blowing velocity distribution to be used in the incorporation of viscous effects into the inviscid method. The inviscid flow solutions made use of four lifting strips, and the viscous flow calculations included boundary-layer calculations on the wing and in the wake, the latter requiring velocities at off-body points in the potential field. This interactive and iterative procedure was repeated until the solutions converged. The lift coefficients were then calculated from the inviscid method for each individual strip and included the contribution of ice protruding beyond the wing contour and the drag coefficients from the boundary-layer calculations.

Figure 6 shows the variation of the calculated lift coefficients as a function of angle of attack. Since the primary purpose of the calculations was to demonstrate the increase in drag due to ice on a tapered wing, the angle of attack range was not extended to stall, which would occur at relatively high angles of attack for low aspect ratio wings. The higher lift coefficient than for the clean wing shown for the two iced wings is due to the normalization with the wing area of the clean wing in both cases. The conclusion from this figure is that lift is not affected by the rime ice accretion for the angle of attack range considered here because the ice shapes along the leading edge of the wing for runs 8 and 11 do not cause premature flow separation on the wing.

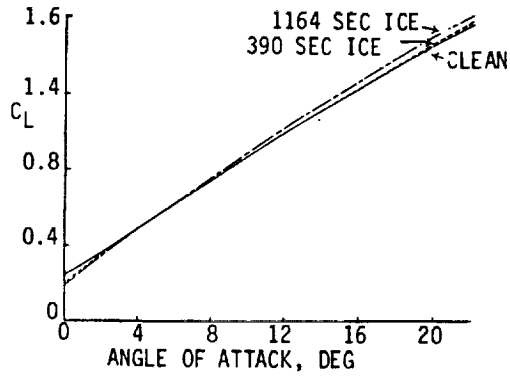

Fig. 6. Effect of leading-edge 390 and 1164 second rime ice on the lift coefficient of a tapered wing for $R = 4.6 \times 10^6$ based on root chord.

The calculated drag coefficients shown in Fig. 7 represent the profile drag of the wing only and do not represent the total drag, since that requires the contribution of the induced drag. The profile drag was calculated sectionwise from the Squire-Young formula based on the resultant velocity at the trailing edge. Comparable results were also obtained from the momentum deficiency in the far wake. Here we see considerable differences between the clean wing and the two iced wings because the Reynolds number is relatively low ($Re = 4.6 \times 10^6$ for the root chord) and

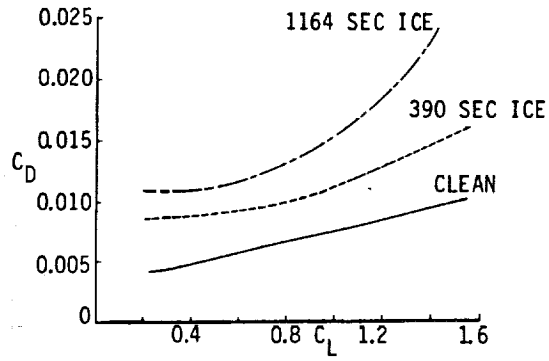

Fig. 7. Effect of leading edge 390 and 1164-second rime ice on the profile drag coefficient of a tapered wing for $R_c = 4.6 \times 10^6$ based on root chord.

there are large regions of laminar flow on the clean wing. The principal contributor to the drag increase for the iced wing is the shift in transition to near the leading edge due to roughness of the iced surface. The contribution of the surface roughness itself to the drag is very small for Run 8 because the extent of ice is small and its shape emulates an airfoil leading edge. The additional drag increase for Run 11 results from the surface roughness spread over a large wetted area increment. The main conclusion that can be drawn from these comparisons is that drag increments obtained between clean and iced airfoils in wind tunnels depend on transition locations on the clean wing. If the Run 8 case represents a wing with transition fixed at the leading edge and the clean wing case is transition free, the observed drag increments from the Run 11 case are quite different from each other. As a corollary, drag increments obtained from wind-tunnel tests may be meaningless without fixing transition or knowing where transition occurs during the tests.

3.6 Results for an Unswept NACA 0012 Wing

Bragg et al.[16] have tested two wings with a simulated ice shape to determine its effect on wing aerodynamic characteristics. They also tested the same wings in clean conditions to establish the base case. Their measurements include selected chordwise pressure distributions, balance data on lift and drag coefficients, and section drag data by wake measurements. Since these measurements were conducted in a wind tunnel and our calculations were to be done for freestream conditions, at first we decided to perform the calculations for the clean unswept wing with the interactive method of Section 3. The inviscid code used seven lifting strips, each with 180 chordwise panels along the semispan.

Figure 8 shows the calculated pressure distributions for $\alpha = 4$ degrees together with the experimental results. The overall agreement is very good. Also shown are the integrated sectional lift coefficients which differ somewhat from case to case, but this is expected from integration of nonsmooth data. Studies are in progress to evaluate the interactive method for the swept clean wing and then apply the method to both unswept and swept wings with ice.

4.0 Calculation of Ice Shapes on Multielement Airfoils

To extend the method developed for analyzing iced airfoils and wings to high-lift configurations, our studies first concentrated on the calculation of ice shapes on the slat of a four-element airfoil shown in Fig. 9. Figure 10 shows the inviscid pressure distribution of the clean four-element airfoil at $\alpha = 0°$. The ice shapes of the first element corresponding to times up to two minutes are shown in Fig. 11 for a time step Δt of one minute. With ice build-up on the first element, the computed pressure distribution build- up remains essentially the same except along the first element. Figure 12 shows the progression of the pressure distributions of the first element with time. As can be seen, the ice accretions cause rapid changes in the pressure distribution with large leading-edge peaks.

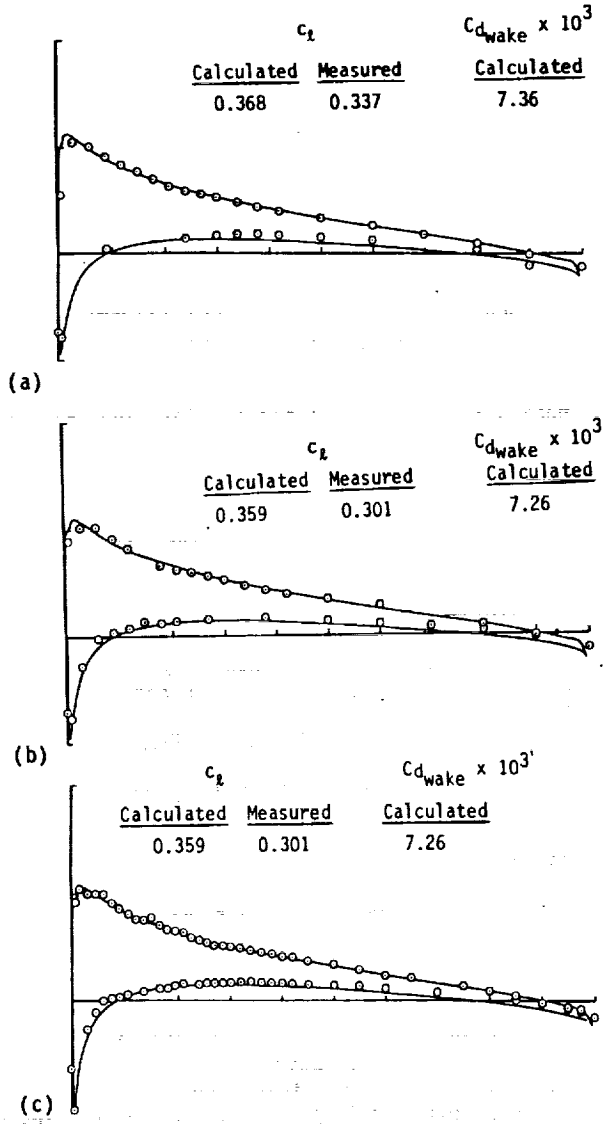

Fig. 8. Comparison of calculated (solid lines) and measured (symbols) results for the unswept clean wing of Ref. 16 at $\alpha = 4°$: (a) y/b = 0.168, (b) y/b = 0.336, (c) y/b = 0.497.

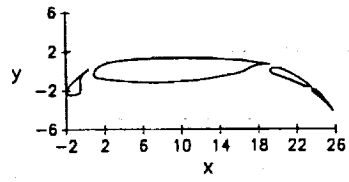

Fig. 9. Geometry of the four-element airfoil.

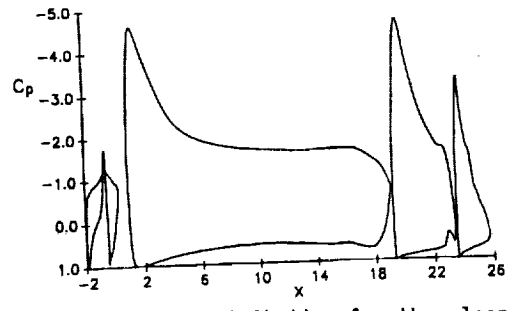

Fig. 10. Pressure distribution for the clean four-element airfoil at $\alpha = 0°$.

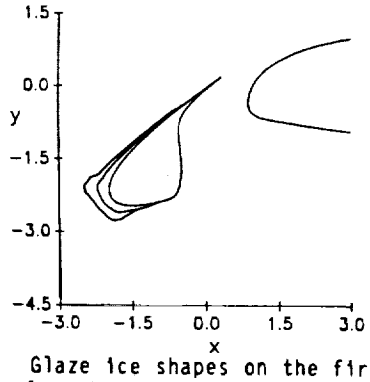

Fig. 11. Glaze ice shapes on the first element of the four-element airfoil at $\alpha = 0°$.

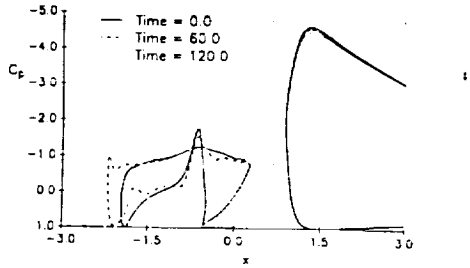

Fig. 12. Pressure distribution along the first element of the four-element airfoil with glaze ice accretion at $\alpha = 0°$.

Very recently, the above method has also been extended to multielement airfoils. Figures 13 to 16 show the pressure distributions and the ice shapes on the first two elements of the four-element airfoil at $\alpha = 4°$ and 6°. The ice shapes correspond to 2 and 5 minutes.

Figures 17 and 18 show the results for the four-element airfoil at $\alpha = 0°$ for a two-minute glaze ice computed by the multielement LEWICE code. Additional studies are in progress and will be reported later.

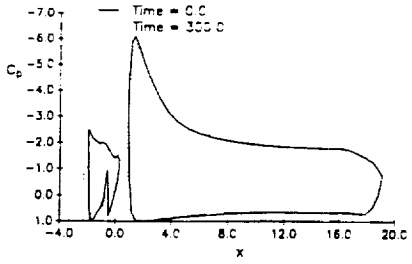

Fig. 13. Pressure distribution for the clean four-element airfoil at $\alpha = 4°$.

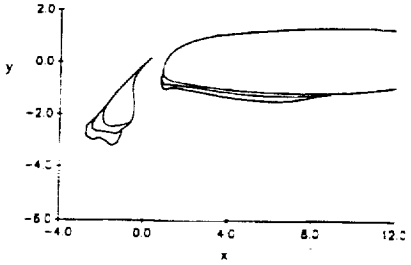

Fig. 14. Glaze ice shapes on the first two elements of the four-element airfoil at $\alpha = 4°$. The ice shapes correspond to 2 and 5 minutes.

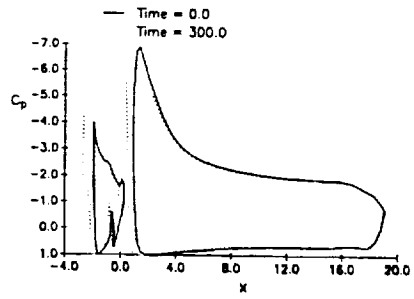

Fig. 15. Pressure distribution for the clean four-element airfoil at $\alpha = 6°$.

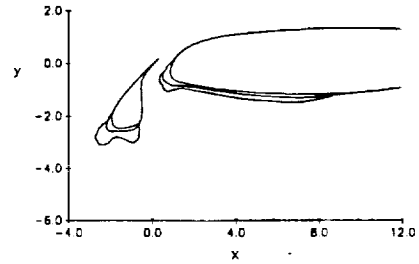

Fig. 16. Glaze ice shapes on the first two elements of the four-element airfoil at $\alpha = 6°$. The ice shapes correspond to 2 and 5 minutes.

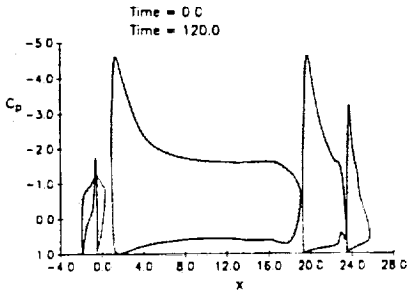

Fig. 17. Pressure distribution for clean and iced four-element airfoil at $\alpha = 0°$.

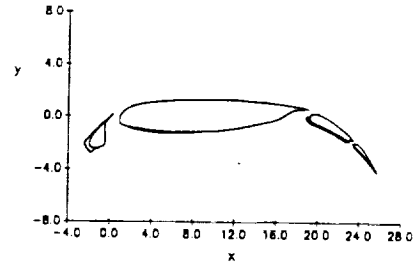

Fig. 18. Computed two-minute glaze ice shapes on a four-element airfoil at $\alpha = 0°$.

5.0 Concluding Remarks

Until recently, the only capability for predicting ice shapes on aerodynamic configurations was limited to single airfoils. With the methods described here and with the method described in Ref. 17 for wings, this capability now includes wings and multielement airfoils. These methods, however, are in their infancy and require improvements and validation with experimental data.

The interactive method for three-dimensional flows also provides a new capability that, except for the recent work of Ref. 18, did not exist for iced wings. Both methods are, also in the early development stages and require additional work and validation with experimental data.

6.0 References

1. Shaw, R.J., Potapczuk, M.G. and Bidwell, C.S., "Predictions of Airfoil Aerodynamic Performance Degradation Due to Icing," in Numerical and Physical Aspects of Aerodynamic Flows IV (ed. T. Cebeci), p. 19, Springer-Verlag, Berlin-Heidelberg, 1990.

2. Ruff, G.A. and Berkowitz, B.M., "User's Manual for the NASA Lewis Ice Accretion Code (LEWICE)," NASA CR-185129, May 1990.

3. Cebeci, T. Chen, H.H. and Alemdaroglu, N., "Fortified LEWICE with Viscous Effects," Journal of Aircraft, Vol. 28, No. 9, pp. 564-571, Sept. 1991.

4. Cebeci, T., "Calculation of Flow Over Iced Airfoils," AIAA J., Vol. 27, p. 853, 1989.

5. Shin, J., Berkowitz, B., Chen, H.H. and Cebeci, T., "Prediction of Ice Shapes and Their Effect on Airfoil Performance," AIAA Paper 91-0264, Jan. 1991.

6. Shin, J., Chen, H. H. and Cebeci T., "A Turbulence Model for Iced Airfoils and Its Validation," AIAA Paper No. 92-0417, Jan. 1992.

7. Britton, R., "Development of an Analytical Method to Predict Helicopter Main Rotor Performance in Icing Conditions," AIAA Paper No. 92-0418, Jan. 1992.

8. Cebeci, T., Jau, J. and Vitiello, D., "An Interactive Boundary-Layer Approach to Multi-element Airfoils at High Lift," AIAA Paper No. 92-0404, Jan. 1992.

9. Cebeci, T., Chen, H. H., Kaups, K. and Schimke, S., "Analysis of Iced Wings," AIAA Paper No. 92-0416, Jan. 1992.

10. Potapczuk, M.G. and Bidwell, C.S., "Numerical Simulation of Ice Growth on a MS-317 Swept Wing Geometry," AIAA Paper No. 91-0263, 1991.

11. Bidwell, C.S., "Icing Characteristics of a Natural Laminar Flows, a Medium-Speed, and a Swept Medium-Speed Airfoil," AIAA Paper 91-0447, Jan. 1991.

12. Hess, J.L., "The Problem of Three-Dimensional Lifting Flow and Its Solution by Means of Surface Singularity Distribution," Computer Methods in Applied Mechanics and Engineering, Vol. 4, pp. 283-319, 1974.

13. Veldman, A.E.P., "New Quasi-Simultaneous Method to Calculate Interacting Boundary Layers," AIAA Journal, Vol. 19, p. 679, 1981.

14. Cebeci, T., Khattab, A.A., Chen, H.H. and Chen, L.T., "An Approach to the Design of Wings: The Role of Mathematics, Physics and Economics," AIAA Paper No. 92-0286, Jan. 1992.

15. Bradshaw, P., Cebeci, T. and Whitelaw, J.H., Engineering Calculation Methods for Turbulent Flows, Academic Press, London, 1981.

16. Bragg, M., Khodadoust, A., Soltani, R., Wells, S. and Kenko, M., "Effect of a Simulated Ice Accretion on the Aerodynamics of a Swept Wing," AIAA Paper No. 91-0442, 1992.

17. Potapczuk, M.G., "Navier-Stokes Analysis of Airfoils with Leading-Edge Ice Accretions," Ph.D. Dissertation, The University of Akron, May 1989.

18. Kwon, O.J. and Sankar, L.N., "Numerical Study of the Effect of Icing on Fixed and Rotary Wing Performance," AIAA Paper 91-0662, 1991.